Department of Electrical
and
Computer Systems Engineering

Technical Report
MECSE-22-2005

INTEGRATED PHOTONICS: PART I - MODELING OF SYMMET ASYMMETRIC TRAVELLING WAVE ELECTRODES FOR ULTR OPTICAL MOULATORS

L.N. Binh

MONASH
UNIVERSITY

INTEGRATED PHOTONICS: PART I

MODELING OF SYMMETRIC AND ASYMMETRIC TRAVELLING WAVE ELECTRODES FOR ULTRA-BROADBAND OPTICAL MOULATORS

Le Nguyen Binh
Department of electrical and Computer Systems Engineering, Monash University, Clayton Victoria 3168 AUSTRALIA
e-mail: le.nguyen.binh@eng.monash.edu.au

Abstract

Broadband optical modulators, especially the $LiNbO_3$ interferometric types, are currently important in the generation of advanced modulation formats for ultra-high speed ultra-long haul optical transmission systems. In these devices the effectiveness of the generating of the travelling electric field for the electro-optic interaction is very critical. This paper presents a finite difference analysis of asymmetric travelling wave electrodes normally integrated over the interferometric optical waveguide structures for broadband intensity modulation. The effects of the tilt of the electroplated thick electrodes on the device bandwidth are analysed. We have also used the travelling wave electric field model to calculate the electro-optic overlap integral . Key features in optimising the overlap integral are studied to design modulators with low half-wave voltage, V_π can be realised.

Keywords: Optical modulators, optical communications, microwave travelling electrode, mm-wave, integrated photonics

TABLE OF CONTENTS

LIST OF FIGURES

1 Introduction

Optical transmission at ultra-high bit rate up to 40 Gb/s and multiplexing of several optical channels are becoming the standard deployment of dense division wavelength multiplexing (DWDM) optical networks in certain strategic information transport routes. Different modulation formats have been investigated over the last decade in order to increase the transmission capacity and reducing the linear dispersion effects and nonlinear induced effects. In the ultra-high speed transmission systems the external modulators play a vital role. Of particular interest are the modulators in lithium niobate and other compound semiconductor integrated optical devices[1]. The modulators can be single or asymmetric electrode or dual (balanced or symmetric) electrode structures which require precision in the design and fabrication.

Several published works have outlined the important steps and considerations involved to achieve efficient design of travelling wave electrodes. The major part of the design calculations were based upon adopted empirical model that was derived from the combination of the Quasi TEM analysis and the Green function method. The empirical model, despite being impressive in its ability to facilitate the design calculation, does not provide the modulating electric field that is mandatory in calculating the electro-optical overlap integral. More importantly, it does not take into account of the more subtle structural factors such as the wall angle of the gold plated electrode [21]. Most analysis such as the conformal mapping technique [1], the Green function method [4-5] or the method of images [3,15], either assume an infinitely thin electrodes or assume the wall angle of the electrode to be 90°. But when very thick electrodes, typically in the range of 10 to 20 μm

[1] Readers can refer to several papers presented in on advanced modulation formats in the proceedings of the 2004 IEEE/LEOS Workshop on Advanced Modulation Formats, San Francisco CA. ISBN 0-7803-8425-3 in which the Mach Zehneder interferometric modulators have been extensively employed

[20,21], are employed to achieve broadband operation capable of handling bandwidth of more than 40 GHz, the assumption of perfectly vertical wall angle is no longer valid. In practical devices, after the gold electroplating, the electrode would assume a trapezoidal shape as shown in ***Figure 1***.

The wall angle of the electrode in fact has a rather significant influence on the value of effective microwave index n_m and characteristic impedance Z. It is therefore important to take such structural effect of the electrodes into consideration in the design of travelling wave electrodes. Chung *et al.*[4,5] has modelled the electric field of the electrodes with the Green function method but their analysis does not take the effect of the wall angle into account. This has led to the limitation of the reported empirical model.

Electrode structural factors such as this can only be modelled by a more robust numerical formulation such as the finite element method [12-13, 19-20] or the finite difference method [18]. We have decided to employ the finite difference method to solve the anisotropic Laplace Equation. Finite differencing is impressive in its relatively straight forward analysis. In the workstation environment that has virtual memory support, this scheme can warrant a rather impressive result in a relatively short time without tedious mathematical analysis and programming involved in those of the finite element method. The non-uniform grid allocation is used to economise the requirement of computer storage capacity.

The next section outlines the numerical formulation of the non-uniform mesh finite difference scheme to solve the anisotropic Laplace equation under the quasi-TEM assumption of the microwave mode. Based on this numerical model, we have developed an application program named FDTWEA (Finite Difference Travelling Wave Electrodes Analysis) to compute the electrode parameters Z, n_m, the modulating field, E_x and E_y, and the overlap integral, Γ. Our simulated results will be compared with published results to verify the validity of our FDTWEA simulator. The simulator is also employed to study the effect of the wall tilted angle on electrode design.

2 Numerical Formulation

2.1 Solving the anisotropic Laplace equation

As mentioned in the previous section, the travelling wave electrodes are miniature transmission where a quasi-TEM wave transmission is assumed, hence, the electric field calculation is reduced to a two-dimensional electrostatic field calculation. The static field can in fact be worked out by solving the well known Laplace Equation. Since the $LiNbO_3$ substrate and the SiO_2 dielectric are involved, we have an anisotropic case at hands. We would assume a Z-cut orientation of the $LiNbO_3$ crystal. This would mean that the permittivity tensor is diagonal [1] and the electrostatic potential V is essentially the solution of the anisotropic Laplace equation written as follows:

$$\frac{\partial}{\partial x}\left(\varepsilon_x \frac{\partial V}{\partial x}\right) + \frac{\partial}{\partial y}\left(\varepsilon_y \frac{\partial V}{\partial y}\right) = 0 \qquad (1)$$

The equation ca be numerically solved by the finite difference method using a non-uniform mesh allocation scheme which is employed in order to economise computer memory requirement and hence computing time. Denser mesh is allocated at the edges of the electrode and also the buffer layer area so that the effect of the edge field can be modelled more accurately. Points that are further away from the electrode can be modelled with a coarser mesh. The steps involved in setting up the difference equation [19] can be formulated as follows:

Consider a general electrode structure as shown in ***Figure 2***(a). The grid points are placed along dielectric boundary. Since the electrode structures for our consideration involve only three dielectric medium, namely, the air, the SiO_2 thin coated layer and the $LiNbO_3$ substrate. With $LiNbO_3$ being the anisotropic medium, the transition of different dielectric medium occurs only in the y direction. Therefore, it suffices to analyse the two layers of dielectric medium as shown in ***Figure 2***(b) to formulate our difference equations.

Consider a mesh point P along the boundary and four other points surrounding it, namely, A, B, C, D. The point in between AP, BP, CP and DP are labelled 1, 2, 3 and 4, while their

respective grid sizes are h_a, h_b, h_c and h_d. The electrical potential at each point are V_P, V_A, V_B, V_C and V_D, respectively. K_{e1} and K_{e2} are the dielectric constants of the medium.

At point 1,

$$\frac{\partial V}{\partial x} \approx \frac{V_P - V_A}{h_a} \tag{2a}$$

At point 2,

$$\frac{\partial V}{\partial x} \approx \frac{V_B - V_P}{h_b} \tag{2b}$$

At point 3,

$$\frac{\partial V}{\partial y} \approx \frac{V_C - V_P}{h_c} \tag{2c}$$

At point 4,

$$\frac{\partial V}{\partial y} \approx \frac{V_P - V_D}{h_d} \tag{2d}$$

With the assumption that half of the flux flows in medium 1 and the other half flows in medium 2, we have

$$\left(\varepsilon_x \frac{\partial V}{\partial x}\right)_{PB} = \frac{\frac{1}{2}(Ke_{1x} + Ke_{2x}) \cdot (V_B - V_P)}{h_b} \quad \text{along segment PB} \tag{3a}$$

$$\left(\varepsilon_x \frac{\partial V}{\partial x}\right)_{AP} = \frac{\frac{1}{2}(Ke_{1x} + Ke_{2x}) \cdot (V_P - V_A)}{h_a} \quad \text{along segment AP} \tag{3b}$$

$$\left(\varepsilon_y \frac{\partial V}{\partial y}\right)_{PC} = \frac{Ke_{2y} \cdot (V_C - V_P)}{h_c} \quad \text{along segment PC} \tag{3c}$$

$$\left(\varepsilon_y \frac{\partial V}{\partial y}\right)_{DP} = \frac{Ke_{1y} \cdot (V_P - V_D)}{h_d} \qquad \text{along segment DP} \qquad (3d)$$

From (1) we have

$$\frac{\left(\varepsilon_x \frac{\partial V}{\partial x}\right)_{PB} - \left(\varepsilon_x \frac{\partial V}{\partial x}\right)_{AP}}{\frac{1}{2}(h_a + h_b)} + \frac{\left(\varepsilon_y \frac{\partial V}{\partial y}\right)_{PC} - \left(\varepsilon_y \frac{\partial V}{\partial y}\right)_{DP}}{\frac{1}{2}(h_c + h_d)} = 0 \qquad (4)$$

By substituting (3) into (4), we get

$$K_A V_A + K_B V_B + K_C V_C + K_D V_D - K_P V_P = 0 \qquad (5)$$

which is essentially a five-point difference equations with

$$K_A = \frac{Ke_{1x} + Ke_{2x}}{hb \cdot (ha + hb)} \qquad (6a)$$

$$K_B = \frac{Ke_{1x} + Ke_{2x}}{ha \cdot (ha + hb)} \qquad (6b)$$

$$K_C = \frac{Ke_{2y}}{\frac{1}{2} hc \cdot (hc + hd)} \qquad (6c)$$

$$K_D = \frac{Ke_{1y}}{\frac{1}{2} hd \cdot (hc + hd)} \qquad (6d)$$

$$K_P = K_A + K_B + K_C + K_D \qquad (6e)$$

Consider the following schematic diagram for the general structure of a device to show how the boundary conditions should be handled.

In the air and the SiO_2 buffer layer, we have homogeneous medium where $Ke_{1x} = Ke_{2x} = Ke_{1y} = Ke_{2y}$. So we have

$$K_A = \frac{1}{h_a \cdot (h_a + h_b)} \tag{7a}$$

$$K_B = \frac{1}{h_b \cdot (h_a + h_b)} \tag{7b}$$

$$K_C = \frac{1}{h_c \cdot (h_c + h_d)} \tag{7c}$$

$$K_D = \frac{1}{h_d \cdot (h_c + h_d)} \tag{7d}$$

Along the buffer and crystal boundary, $Ke_{1x} = Ke_{1y} = \varepsilon_b$, $Ke_{2x} = \varepsilon_x$, $Ke_{2y} = \varepsilon_y$, therefore

$$K_A = \frac{\varepsilon_b + \varepsilon_x}{h_a \cdot (h_a + h_b)} \tag{8a}$$

$$K_B = \frac{\varepsilon_b + \varepsilon_x}{h_b \cdot (h_a + h_b)} \tag{8b}$$

$$K_C = \frac{2\varepsilon_y}{h_c \cdot (h_c + h_d)} \tag{8c}$$

$$K_D = \frac{2\varepsilon_b}{h_d \cdot (h_c + h_d)} \tag{8d}$$

In the $LiNbO_3$, $Ke_{1x} = Ke_{1y} = \varepsilon_b$, $Ke_{2x} = \varepsilon_x$, $Ke_{2y} = \varepsilon_y$, therefore

$$K_A = \frac{2\varepsilon_x}{h_a \cdot (h_a + h_b)} \tag{9a}$$

$$K_B = \frac{2\varepsilon_x}{h_b \cdot (h_a + h_b)} \tag{9b}$$

$$K_C = \frac{2\varepsilon_y}{h_c \cdot (h_c + h_d)} \tag{9c}$$

$$K_D = \frac{2\varepsilon_y}{h_d \cdot (h_c + h_d)} \tag{9d}$$

For grid points on the electrodes, we have K_A=K_B=K_C=K_D=0, K_P=1. With a large enough problem space of approximately 400×400 μm, we can assume that the electric field along the window boundary to be zero. For the potential, it is essentially a Neumann boundary condition [19, 30] problem.

For the upper window boundary, we have

$$K_A V_A + K_B V_B + 2K_C V_C - K_P V_P = 0 \tag{10}$$

For the left hand window boundary, we have

$$2K_B V_B + K_C V_C + K_D V_D - K_P V_P = 0 \tag{11}$$

For the top left hand corner, we have

$$2K_B V_B + 2K_C V_C - K_P V_P = 0 \tag{12}$$

The rest of the windows are just the permutation of the boundary conditions outlined above. Incorporating the boundary conditions into the difference equations, we can have a set of difference equations derived from each grid point. This set of linear equations takes the form of

$$\mathbf{A}.\mathbf{u}=\mathbf{b} \tag{13}$$

where **A** is the coefficient matrix, **u** is the vector that contains the potential, V of each grid point, while **b** is the vector that assumes the right hand side of (1) which is mostly zero except for the grid points on the electrodes which take up the value of the potential on the relevant electrodes. The following is an example of a typical matrix equation for a problem space which contains nine points like those shown in ***Figure 2***. We would assume that the grid point for j=2 which has the potential V_4, V_5, and V_6 falls on the electrode and assumes a normalised potential of 1V.

The coefficient matrix is known as the tri-diagonal matrix with fringes. The matrix elements p, a, b, c and d for each point correspond to the coefficient K_p, K_A, K_B, K_c and K_d,

respectively. Take note that for points 7, 8 and 9 which fall on the electrode, K_p=1 while K_A, K_B, K_c and K_d are all zero.

The difference equation can be solved by means of the more conventional Successive Over-relaxation Method (SOR) [19,30]. This method, however, requires a good initial guess and a good estimate of the relaxation factor in order to have a reasonable rate of convergence.

With the availability of ITPACK NSPCG[31] , the matrix can be solved relatively quickly and easily with good accuracy. ITPACK matrix solver applies various accelerators and preconditioners in solving the matrix. For a band matrix, we need to store only the nonzero elementswhich would greatly economise the computer memory usage. In the application programs developed, the Othormin (Omin) accelerator and Incomplete Cholesky (IC) preconditioner is used [31]. The solution of the anisotropic Laplace equation would then enable us to calculate various properties of the microwave electrodes.

2.2 Line Capacitance, Characteristic Impedance and Microwave Effective Index

The whole purpose of carrying out the above numerical formulation is eventually to compute the relevant travelling wave electrodes parameters such as the characteristic impedance Z and the microwave effective index n_m. The characteristic impedance is given as

$$Z = \frac{1}{c\sqrt{CC_o}} \tag{15}$$

while the microwave effective index n_m is

$$n_m = \sqrt{\frac{C_o}{C}} \tag{16}$$

where C is the capacitance per unit length of the transmission line with the dielectric medium, while C_0 is the capacitance per unit length for the air filled medium, with c being the speed of light in vacuum.

To compute these quantities, we will need to compute the line capacitance C and C_0 of the transmission line in the dielectric medium and air, respectively. To obtain the capacity it is prerequisite to determine the charges on the conductors. This may be found by the Gauss theorem[26], requiring the integration of the normal component of the electric flux over a surface enclosing the hot electrode as shown in ***Figure 3***.

Forming this surface by lines joining the ***Figure 4*** nodal points drawn parallel to the coordinate directions, at any point P on this surface, we have

$$D_n = \varepsilon E_n = -\varepsilon \frac{\partial V}{\partial n} \tag{17}$$

where D_n is the normal component of the electric flux, E_n is the normal component of electric intensity, and n is the normal coordinate, which for a square box would be x and y.

The potential at P may be expressed numerically in terms of the known potentials V_A and V_b on each side of it. For irregular mesh as shown in ***Figure 2*** we have,

$$\frac{\partial V}{\partial x} = \frac{V_B - V_A}{h_b + h_a} \tag{18}$$

$$\frac{\partial V}{\partial y} = \frac{V_C - V_D}{h_c + h_d} \tag{19}$$

It is now easy to apply the Gauss' Theorem. Thus, if the surface (which can be any arbitrary shape) containing the hot conductor consists of s straight line segments each containing r nodes (in our case, we take the integration over a square box which means s=4), the charge per unit length normal to the cross section would then be given by

$$Q = \varepsilon_r \varepsilon_o l \sum_{s}{}' \sum_{P=1}^{4} \left(\frac{\partial V}{\partial n} \right)_P \tag{20}$$

where the apostrophe sign is used to indicate that the first and last terms in the summation are halved, which is seen to be equivalent to integration by the trapezoidal rule, l is the length of the infinitesimal segment of the integration path. For uniform discretisation, l is

essentially the grid size h. For our non-uniform scheme, l is assumed to be either $(h_a+h_b)/2$ or $(h_c+h_d)/2$ depending on either a horizontal or vertical line segment over which the summation is taken. The value of the relative permittivity, ε_r depends on which dielectric medium point P falls onto. For instance, when we sum the derivative along the first horizontal line segment (s=1), the segment falls completely in the air, so ε_r=1.0. If the summation is done on the line segment number 3, which is in the $LiNbO_3$ crystal, $\varepsilon_r = \varepsilon_z$=43. The vertical summation (s = 2, 4) however need to be dealt with care because it involves dielectric medium transition. For points which is entirely in the air, SiO_2 and $LiNbO_3$, the relative permittivities are ε_a =1.0, ε_b=3.9 and ε_x=28, respectively. However, for points that fall on the buffer air interface, we assume half of the flux pass through each medium. So for air-SiO_2 interface, $\varepsilon_r=(1+\varepsilon_b)/2$. Whereas for the SiO_2-$LiNbO_3$ interface, $\varepsilon_r=(\varepsilon_b+\varepsilon_x)/2$.

From the charge capacity, it follows that

$$C = \frac{Q}{V_t} \tag{21}$$

where V_t is the potential difference between the conductors, which we would assume to be unity to simply our calculations. To obtain C_o, we will need to solve the Laplace Equation for the transmission line in the air filled medium without the dielectric and go through similar process to work out the charge capacity and hence the capacitance. Once both C_o and C are determined, the characteristic impedance, Z and the microwave effective index, n_m can be determined by (15) and (16).

2.3 Electric field E_x and E_y and the overlap integral

Once the electric potential V is solved, the electric field can be calculated relatively easily. Essentially, the electric fields E_x and E_y are the derivatives of V in both the x and y directions. This can be computed as follows:

$$E_x = \frac{\partial V}{\partial x} = \frac{V_B - V_A}{(h_a + h_b)} \tag{22}$$

$$E_y = \frac{\partial V}{\partial y} = \frac{V_C - V_D}{(h_c + h_d)} \tag{23}$$

Once the electrical field is determined, calculation of the overlap integral is relatively straight forward. The overlap integral, Γ is defined as [15,16] :

$$\Gamma = \frac{g}{V}\iint |E_o(x,y)|^2 E_m(x,y)dxdy \tag{5.24}$$

where $|E_o(x,y)|^2$, and E_m is the electrical field of the electrodes. The choice of E_x or E_y depends on the crystal orientation and the polarisation of the optical field. The normalised optical field intensity profile assumes a Hermitian-Gaussian profile which is defined as [15,16]

$$|E_o(x,y)|^2 = \frac{4y^2}{w_x w_y^3 \pi}\exp\left[-\left(\frac{x-p}{w_x}\right)^2\right]\cdot\exp\left[-\left(\frac{y}{w_y}\right)^2\right] \tag{25}$$

where the 1/e intensity width and depth are $2w_X$ and $1.376w_Y$, respectively, and p is the peak position of the optical field in the lateral direction. w_x and w_y are dependant on waveguide fabrication parameters and can either be determined experimentally or by the SVMM mode modelling program. For calculation purpose, the values of w_x and w_y that we adopted are 2.5 μm and 2.2 μm respectively [16]. The ability to work out Γ simply means that we can calculate V_π easily.

3 Simulation Results and Discussion

3.1 Grid Allocation and General Performance

To acquire accurate results, we need to discretise the problem space judiciously. The followings are the contour plots of the potentials for CPW, ACPS and CPS electrode structures. The contour plots are essentially the solution of the Laplace equations. In all the three structures in the plots, w=10 μm, g=15 μm, t=3 μm and t_b=1.2 μm.

We have also shown the relevant electric fields E_x, and E_y of each structure to have an idea of what the field profile is like. The electric field shown in the graphs are calculated at the first micron of the $LiNbO_3$ substrate right underneath the SiO_2 buffer layer. The electric field is effectively the rate of change of the potential. The horizontal field, E_x is strongest in between the gaps while the vertical field, E_y is strongest along the hot electrodes in all structures. From these plots, we could see that the push pull operation can be achieved most efficiently by the horizontal field, E_x of a CPW structure for the X-cut Y-propagating device. Another configuration would be to place the waveguides directly underneath the CPS electrodes to make full use of the vertical field, E_y. This, of course, would correspond to a Z-cut device. The CPS structure, however, exhibits a high propagation loss[20] and is therefore seldom employed. A common configuration for Z-cut device is to place one waveguide under the hot electrodes and the other at the edge of the ground plane in either the CPW or ACPS structure. The vertical field E_y is employed in such configuration. This however can not be considered as a full push-pull operation because the waveguide underneath the ground plane sees only on-half of the field seen by the waveguide under the hot electrode.

From the above contour plots and the field plots, we can see that the strongest field exists around the edges of the electrodes, within the SiO_2 buffer layer underneath the hot electrodes and also in the gap between the electrodes. It is therefore a good idea to allocate denser grids around these areas. For points which are further away from these regions, we can allocate a coarser grid. From our experience, a grid size as small as 0.05 μm to 0.2 μm at around the electrode edges, the gap and buffer region, up to larger grid size of 8 to 10 μm for points where the electric field has decayed substantially will warrant a accurate calculation result. The grid size is specified via a grid allocation file. If the file is not specified, FDTWEA generates one automatically using its default grid allocation scheme suitable for the relevant electrode structure. This grid allocation file can then be modified for further simulation if necessary. We find that a problem space of around 400 by 400 μm is sufficient to assume a metal box boundary condition. An average grid size for that problem space would be around 300 by 200 points. With the band storage mode employed

by the matrix solver and a work station environment, such dense grid mesh can be supported without any problem.

3.2 Accuracy assessment of FDTWEA

3.2.1 General comparison

To assess the validity of our results, we compare the values of Z and n_m with published experimental results. The comparisons are tabulated in ***Table 1***.

From ***Table 1***, we can gather that the simulated results of FDTWEA for both the CPW and ACPS electrodes compare well with the measured results published by Chung *et al.*[5]. In this calculation, we calculated the Z and n_m values for the buffer layer that varies between 0.6-0.85 because these two values of t_b are determined from the fabrication tolerances of the test devices. It turns out that both the calculations have agreed very well with the measured values.

There seems to be a discrepancy in our calculated Z value of the ACPS structure compared to the one reported by Korotky *et al.*[22] . However, it was not mentioned in their paper how they obtained the value of Z to be 35Ω. We have therefore made the assumption that the calculations in Ref[22] have not taken the thickness of the electrodes into account. So we recalculate the impedance with the assumption of an infinitely thin electrode. As it turns out, the recalculated impedance is 3315, which agrees well with their reported value.

Our third modelling is based on the experimental results reported by Chuang *et al.*[16] Our simulated results agree closely with their theoretical calculations which are based on the method of image. However, the measured results differ slightly from that of the theoretical predictions. The characteristic impedance measured by using the TDR (Time Domain Reflector) and NA (Network Analyser) techniques were 49.8Ω and 47.1Ω, respectively. The small discrepancy is possibly due to a slightly thicker SiO_2 buffer layer coated in the experiment.

3.2.2 FDTWEA versus spectral domain analysis

Our simulations are then compared further by emulating the calculations by spectra domain analys as reported by Kawano et al[9]. ***Figure 11***(a) and (b) below show the comparison of the two simulations. Initially, we calculated the parameter based on the electrode parameters of t=4 μm, t_b=0-1.5 μm, w=8 μm and g=30 μm. Our results, however, have seemed to underestimate both the values of Z and n_m. It was later realised that the spectral domain analysis of Kawano *et al.* may not have taken the thickness of the electrode into account. So we recalculate Z and n_m with the assumption of a zero thickness electrodes. Results of our calculation turn out to be almost a perfect match to that of Kawano *et al*. This has clearly implied that the spectral domain analysis of Kawano *et al* [9] did not take into account the effect of the electrode thickness. Such limitation does not exist in our present finite difference analysis.

3.2.3 FDTWEA versus finite element method

We further verify our calculation program by comparing the value of n_m with the simulation result of very thick electrodes carried out by Gopalakrishanan *et al.*[19] which is based on the finite element calculation. The result of the comparison is shown in Figure 12. The calculations are intended to show how the thickness of the electrodes can significantly improve the electrical and optical velocity matching. Thick electrodes that are in the range of 10-20 μm are employed. From Figure 12, we can see that our calculations which are based on the finite difference method agrees to within 0.5% with its Finite Element counterpart. We have employed the grid size of 0.125 μm along the wall of the thick electrodes in our calculations. Each calculation takes approximately 3 to 4 minutes to complete on a standard PC Window 2000 operating system.

This result is encouraging because the finite element method has always been considered to be one of the most superior numerical modelling technique. As it turns out, our finite difference scheme has achieved similar level of accuracy in a relatively straightforward numerical analysis.

3.2.4 Assessment remarks

Our assessment so far has shown that the finite difference scheme that we adopted is capable of calculating the travelling wave electrode parameters, namely Z and n_m with great precision. All the calculations have been consistent with both the simulations and measured data reported by various authors. Amongst the comparisons that we have made, the results that compare favourably with the finite element method is the one which is most promising. It has simply verified the validity of our numerical model. FDTWEA, with its verified precision would therefore be a useful tool to provide a good quantitative measure in the design and analysis of travelling wave electrodes.

4 The Overlap Integral, Γ

The theoretical analysis of overlap integral computation has already been outlined in section 2.3. In this section, we will show some of the calculation result and discuss a few issues on the electrical-optical overlap integral. As mentioned earlier, to compute the overlap integral, we need the normalised optical intensity field profile, which is a Hermittion-Gaussion profile as characterised by (25). We rewrite this equation below for reference purposes.

$$\left|E_o(x,y)\right|^2 = \frac{4y^2}{w_x w_y^3 \pi}\exp\left[-\left(\frac{x-p}{w_x}\right)^2\right]\cdot\exp\left[-\left(\frac{y}{w_y}\right)^2\right] \qquad (25)$$

The mode size of the optical field plays an important role in maximising Γ. In Eq. 25, the variables that characterise the mode size are w_x and w_y, which is twice the 1/e modal width and 1.376 times the 1/e modal depth. w_x and w_y can be modelled with a finite element of difference with ease and not given here or by experimentally measured the mode size. Γ is also influenced by the relative position of the optical mode with respect to the hot electrodes. All the attributes that affect the value of Γ can be easily modelled by FDTWEA. For illustration purposes, we will calculate Γ of the ACPS electrodes and study the effects of various factors that can influence its value.

Figures 13 and 14 both show the variations of the overlap integral, Γ as the peak position of the optical mode, p shift from one end of the electrodes to the other end. The plots also

show us quantitatively how the size of the optical mode can affect the Γ. As expected, a tighter confined mode would gives a higher value of Γ. It is therefore important to fabricate a Ti:$LiNbO_3$ that can give the smallest possible mode size.

Apart from having a tightly confined optical mode, the relative position of the optical waveguide with respect to the electrodes is also extremely important to provide a maximum electro-optic effect. When we employ narrow electrode where the electrode width is comparable to the size of the waveguide, then it would be a good idea to place the waveguide directly underneath the electrode to utilise the strong edge field from both side of the electrode. This has been shown in the above plots where maximum Γ is obtained when the position of the optical mode is centred underneath the electrode. However, for an electrode structure which is much wider, the preferred position would be just inside the end of the electrode closer to the gap. This is shown in Figure 15 when a 30 μm wide electrode is employed.

Figure 14 shows that maximum overlap integral can be achieved by exploiting the higher edge field by centring the waveguide x~135 μm. Having the optical waveguide right at the centre of the electrode would be an inefficient design.

Figure 15and ***Figure 16*** show how the thicker buffer layer can impede the electro-optic effect. Although a thicker buffer layer has the advantage of a lower conductor loss and also significantly improves the velocity match, there is a trade off involved because the overlap integral will be lower, which can therefore lead to a higher V_π.

We can see that without the buffer layer, Γ assumes a much higher value. Unfortunately, having no buffer layer would imply a much higher optical-electrical velocity mismatch.

Essentially, the position of the optical waveguide with respect to the electrode will need to be considered before fabricating the actual device. It is also important to have a quantitative measure of the effect SiO_2 thickness on the overall performance of the device. We have shown that the FDTWEA can provide a measure that would greatly facilitate the design of travelling wave electrodes.

5 Electrodes in an enclosure and tilted feature

In previous sections, we have used FDTWEA to analyse various rudimentary design parameters of travelling wave electrodes. In this section, we will show how it can also be employed to study other more innovative electrode structure and handle problem of greater complexity in the travelling electrode design. We choose to study the shielded phase velocity-matching travelling wave electrode structure proposed by Kawano *et al.*[11-12] and also the electrode wall angle problem which is looked into by Gopal *et al.*[21]

5.1 Shielded Phase Velocity Matching Travelling Wave Electrode.

Figure 18 is a schematic view of the proposed z-cut Ti:$LiNbO_3$ Mach-Zehnder optical modulator by Kawano *et al.*[11-12]. To reduce the phase-velocity mismatch between the microwave and optical wave, a shielding plan was introduced to the CPW electrode structure. The centre conductor width *w* was set small to obtain high modulation efficiency. Further more, a thick buffer layer was effectively employed to increase the characteristic impedance and to decrease the microwave conductor loss, respectively. The overlaid layer was supposed to be air. The centre conductor width and gap were set to 8 and 15 μm, respectively. ***Figure 19*** shows how the thickness of the overlaid layer, *D* can be controlled to achieve good velocity matching.

From ***Figure 19***, we can see that as the thickness, *D* of the laid layer is reduced, both the values of *Z* and n_m decrease. Significant changes, however, do not happen until *D* is less than 20 μm. A substantial fluctuation in the values of both *Z* and n_m happens when *D* falls below 10 μm. From our calculation, the best velocity matching happens when *D* assumes the value of 4.5 μm. The reported result by Kawano *et al.* suggested an overlaid thickness of 4 μm, which is close to our calculation. For a 20 GHz bandwidth, the voltage-length product of our calculation based on a 4 μm overlaid thickness is 4.2 V/cm compare to their calculation of 13.1 V/cm. The slightly higher voltage-length product in our calculation is due to the reason that we ignore the push pull effect in our overlap integral calculations.

The above calculation has once again shown the usefulness of our finite difference numerical model as an analytical tool. The shielded velocity matched electrode structure,

which can be analytically tedious, has been modelled with ease. This is another example that has confirmed the potential of FDTWEA to analyse more innovative electrode structure. In the next section, the FDTWEA is used to model the effect of the electrode wall angles on the travelling wave properties.

5.2 Thick electrodes with tilted side wall.

The fabrication of travelling wave electrodes is not straight forward. One way of extending the bandwidth of the device is to employ very thick electrodes that are in the range of 10-20 μm. Such thick electrodes, however, do not always assume a rectangular shape. They are more likely to take up a trapezoidal shape like those shown in Figure 20. Such geometrical factor can not be ignored because they certainly have a subtle effect on both the values of Z and n_m. Gopal *et al.*[21] have modelled the effect with their finite element calculation. We shall study the effect of the wall angle with our finite difference model to demonstrate the capability of our numerical model. We would adopt similar electrode structure and dimension similar to that reported by Gopal *et al*. The following figures show the results of our study.

From the above calculations, we can see that the wall angle certainly has a substantial effect on the values of Z and n_m. ***Figure 21*** and Figure 22 show that the trapezoidal shape electrodes will actually lower both the values of Z and n_m. The effect of the wall angle is less severe for thinner electrodes as we can see from the graphs that the difference of the plots for different θ converges as the electrodes become thinner. For thick electrodes, especially those that are greater than 10 μm, the wall angle effect should not be ignored. For example, if we base our design on the assumption of a θ=90° rectangular electrode, then we would use a 20 μm thick electrode for the best velocity match. However, if the fabricated electrodes actually assume a trapezoidal shape with θ=80°, then we would have overestimated the value of n_m for best velocity matching by about 0.2 (which corresponds to almost a 20% loss of the bandwidth that could have been achieved by a 0.01 microwave and optical index mismatched.). The plots shown in Figure 22 suggest that we need only an electrode thickness of around 14 μm to achieve maximum bandwidth. Based on the assumption of an 82° electrode wall angle Gopal *et al.* employed an electrode with a

thickness of 15 μm. It is not difficult to extrapolate from Figure 22 and 23 to see that our finite difference calculation is consistent with their finite element calculation in analysing the rather profound effect of the wall angle.

Again, we have shown another potential application of our finite difference numerical modelling scheme in offering much analytical capability that would be beyond most analytical techniques such as the Green function method[4.5], spectral domain analysis[9], conformal mapping[1], or method of image[3,15]. Undoubtedly, a greater analytical capability would certainly imply a better design in travelling wave electrodes for optical modulators.

6 Concluding remarks

We have in this paper formulated a numerical model that can offer a better analytical and powerful modelling tool. The anisotropic Laplace equation that has been solved by employing finite difference techniques has led to an accurate model of the microwave properties of various electrode structures. A non-uniform grid allocation scheme that is employed to economise the memory usage in the numerical computation has been shown to be efficient without jeopardising the accuracy of the calculated results. An application package FDTWEA (Finite Difference Travelling Wave Electrode Analysis) has been successfully developed as the numerical modelling tool. The calculated values of the characteristic impedance Z and microwave effective index n_m by our program are consistent with several published literatures. The comparison of FDTWEA' calculations with the finite element scheme[19, 20] has been very promising and encouraging because it has shown great consistency between the two computation techniques.

We have also employed FDTWEA to calculate the overlap integral, Γ. Key features in optimising the overlap integral are studied and discussed. The calculation of Γ is useful to ensure that a device with a low half wave voltage, V_π and hence lower power can be realised.

Apart from studying the more common problem, we have also shown the capability of FDTWEA in analysing other more innovative electrode structures by modelling the shielded

phase-velocity matched electrode structure proposed by Kawano *et al.*[9] Our calculations have demonstrated consistency with their simulated and measured data.

Finally, FDTWEA has been employed to analysing the electrode in a more meticulous manner. We have modelled the effects of the trapezoidal shape electrode with the wall angle θ, which is an electrode geometry assumed by most thick electrode (>10 μm) fabricated by present electroplating technique. The results of our model show that the effect of the wall angle should never be ignored when thick electrode is employed to achieve broadband operation. Quantitatively and qualitatively, our study have been shown to be consistent with the work reported by Gopal *et al.*[20] with the finite element technique. The effect of the wall angle is certainly not a trivial one. This effect is not easily or possibly be modelled by most analytical techniques such as Conformal Mapping, Method of Image, Green Function Method or Spectral Domain Analysis. The subtle effect of the wall angle, however, has been modelled in a relatively straightforward manner with FDTWEA, which clearly deserves full credit for its capability.

We have thus developed a more robust numerical model to facilitate the analysis and design of travelling wave electrodes. Our numerical model would be a substantial contribution to the design of travelling wave electrodes for high-speed optical modulators.

7 References

[1] O.G.Ramer, “Integrated Optic Electrooptic Modulator Electrode Analysis”, *IEEE Journal of Quantum Electron.*, vol. QE-18, no.3, March 1982, pp.386-392.

[2] D. Marcuse, “Optimal Electrode Design for Integrated Optics Modulators”, *IEEE Journal of Quantum Electron.*, vol. QE-18, no.3, March 1982, pp.393-398.

[3] C. Sabatier and E. Caquot, “Influence of a dielectric buffer layer on the field distribution in an electrooptic guided wave device”, *IEEE Journal of Quantum Electronics*, vol. QE-22, no. 1, January, 1986, pp. 32-37.

[4] H. Chung, W.S.C. Chang, and E.L. Adler, "Modelling and Optimisation of Travelling-Wave $LiNbO_3$ Interferometric Modulators", *IEEE Journal of Quantum Electron.*, vol. 27, no.3, March 1991, pp.608-617.

[5] H. Chung, W.S.C. Chang, and G.E. Betts, "Microwave Properties of Travelling-Wave Electrode in $LiNbO_3$ Electrooptic Modulators", *IEEE Journal of Lightwave Technology*, vol. 11, no. 8, August 1993, pp.1274-1278.

[6] M. Seino, *et al.*, "20 GHz 3 dB-bandwidth Ti:$LiNbO_3$ Mach-Zehnder modulator", Proc. ECOC '90, pp.999-1002, postdeadline paper, 1990.

[7] R.A. Becker, "Broadband guided wave electrooptic modulators", *IEEE Journal of Quantum Electronics*, vol. QE-20, no. 7, July 1984, pp.723-727

[8] H. J. M. Bélanger and Z. Jakubezyk, "General Analysis of Electrodes in Integrated Optics Electrooptic Devices", *IEEE Journal of Quantum Electron.*, vol. 27, no.2, February 1991, pp.243-251.

[9] K. Kawano *et al.*, "A wide-band and low driving power phase modulator employing a Ti:$LiNbO_3$ optical waveguide at 1.5 μm wavelength", *IEEE Photonics Technology Letters*, vol. 1. no.2, February, 1989, pp. 33-34.

[10] T. Kitoh and K. Kawano, "Modelling and Design of Ti:$LiNbO_3$ Optical Modulator Electrodes with a Buffer Layer, Electronics and Communication in Japan, Part 2, vol. 76, no. 1, 1993, pp.25-34

[11] K. Kawano *et al.*, "New travelling -wave electrode Mach-Zehnder optical modulator with 20GHz bandwidth and 4.7V driving voltage at 1.52", *Electronics Letters*, vol. 25 no. 20, September 28, 1989, pp. 20-21

[12] K. Kawano *et al.*, "Design and fabrication of shielded velocity matched Ti:$LiNbO_3$ optical modulator", *Electronics and communications in Japan*, Part 2, vol. 75, no.3, 1992, pp. 9-19

[13] Z. Pantic and R. Mittra, "Quasi-TEM Analysis of Microwave Transmission Lines by Finite Element Method", *IEEE Trans. Microwave Th. Tech.*, vol. MTT-34, no. 11, november 1986.

[14] Kenji, Kawano, Kazuto noguchi, Tsutomu Kitoh and Hiroshi Miyazawa, "A Finite Element Method (FEM) Analysis of a Shielded Velocity-Matched Ti:$LiNbO_3$ Op;tical Modulator, *IEEE Photonics Technology Letters*, vol. 3, no. 10, October 1991.

[15] Wei-Ching Chuang *et al.*, "A comparison of the performance of $LiNbO_3$ travelling wave phase modulators with various dielectric buffer layers", *J. Opt. Commun*. 14 (1993) 4, pp. 142-148.

[16] C.M Kim and R. Ramaswamy, "Overlap integral factors in integrated optic modulators and switches", *Journal of Lightwave Technology*, vol. 7, no. 7, July, 1989, pp.1063-1070.

[17] E.L. Wooten and W.S.C. Chiang, "Test structures for characterisation of electrooptic waveguide modulators in lithium niobate", *IEEE Journal of Quantum Electronics*, vol. 29, no. 1, January 1993, pp.161-170

[18] N.H. Zhu, Z.Q. Wang, "Comparison of two coplanar waveguide electrodes for Ti:$LiNbO_3$ interferometric modulators", *Optical and Quantum Electronics* **27**, (1995), pp.607-61

[19] Harry E. Green, "The Numerical Solution of Some Important Transmission-Line Problems, *IEEE Transactions on Microwave Theory and Techniques*, vol. MTT-13, no5, September 1965, pp. 676-692.

[20] G.K. Gopalakrishnan *et al.*, "Electrical loss mechanisms in travelling wave $LiNbO_3$ optical modulators", *Electronics Letters*, vol. 28, no. 2 January 16 1992, pp. 207-208.

[21] G.K. Gopalakrishnan *et al.*, "Performance and modelling of broadband $LiNbO_3$ travelling wave optical intensity modulators", *Journal of Lightwave Technology*, vol. 12, no. 10, October, 1994, pp. 1807-1818.

[22] S.K. Korotky *et al.*, "Optical intensity modulation to 40GHz using a waveguide electro-optic switch", *App.lied Physics Letter*, **50**(23), 8 June 1987, pp.1631-1633.

[23] C.M Gee *et al.*, "17 GHz bandwidth electro-optic modulator", *App.lied Physics Letter*, **43**, no. 11, 1 December, 1983.

[24] W. Charczenko *et al.*, "Characterization and simulation of proton exchanged integrated optical modulators with various dielectric buffer layers", *Journal of Lightwave Technology,* vol. 9, no. 1 January, 1991, pp.92-100.

[25] S.Y. Liao, *Microwave Circuit Analysis and Amplifier Design,* Prentice-Hall International Editions.

[26] Kazuhiko Atsuki and Eikichi Yamashita, "Transmission Line Aspects of the Design of Broad Band Electrooptic Travelling-Wave Modulators, *IEEE Journal of Lighwave Technology,* vol. LT-5, no. 3, March 1987. pp. 316-319.

[27] S.Ramo *et al.*, *Fields And Waves In Communication Electronics*, 2nd Edition, John Wiley & Sons, Inc.

[28] Davis & Hoffman, *Fortran 77:A Structured, Discipline Style*, 2nd Edition, McGraw Hill Book Company.

[29] Murray R. Spiegel, *Mathematical Handbook of Formulas and Tables*, Shaum's Outline Series, McGraw hill Book Company.

[30] William H. Press *et al.*, *Numerical recipes-the art of scientific computing*, Cambridge University Press, pp.240-246.

[31] Thomas C. Oppe *et al., NSPCG user's guide version 1.0 - a package for solving large sparse linear systems by various iterative methods*, Center for Numerical Analysis, The University of Texas, Austin.

[32] .Tamir, *Guided-Wave Optoelectronics*, 2nd Edition, Springer Series in Electronics and Photonics 26, Springer-Verlag.

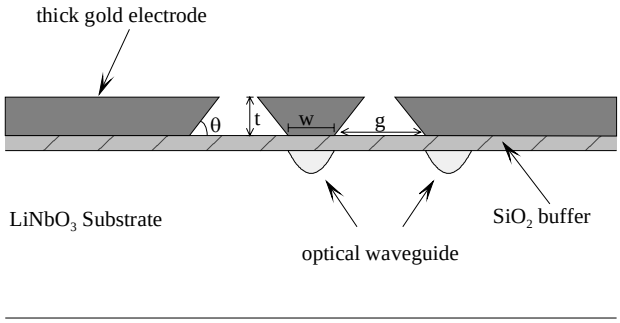

Figure 1: Wall angle of thick electrodes

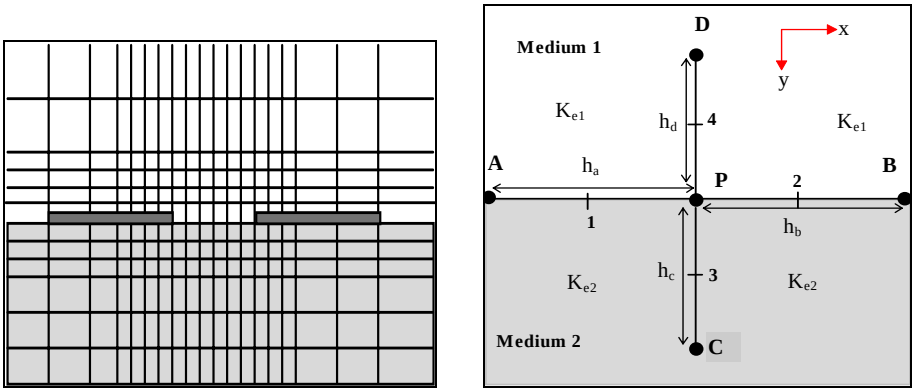

(a) *(b)*

Figure 2: (a) An simple illustration of the non-uniform grid allocation scheme (b): The grid points involved in finite differencing

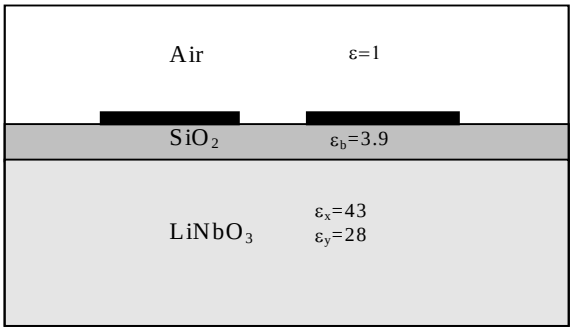

Figure 3: Schematic diagram of dielectric boundary

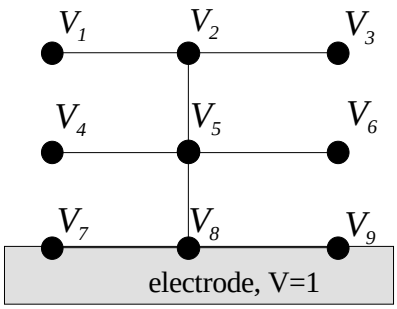

Figure 4: a 3x3 grid spacing

$$\begin{bmatrix} p_1 & b_1 & 0 & c_1 & 0 & 0 & 0 & 0 & 0 \\ a_2 & p_2 & b_2 & 0 & c_2 & 0 & 0 & 0 & 0 \\ 0 & a_3 & p_3 & b_3 & 0 & c_3 & 0 & 0 & 0 \\ d_4 & 0 & a_4 & p_4 & b_4 & 0 & c_4 & 0 & 0 \\ 0 & d_5 & 0 & a_5 & p_5 & b_5 & 0 & c_5 & 0 \\ 0 & 0 & d_6 & 0 & a_6 & p_6 & b_6 & 0 & c_6 \\ 0 & 0 & 0 & 0 & 0 & 0 & 1 & 0 & 0 \\ 0 & 0 & 0 & 0 & 0 & 0 & 0 & 1 & 0 \\ 0 & 0 & 0 & 0 & 0 & 0 & 0 & 0 & 1 \end{bmatrix} \begin{bmatrix} V_1 \\ V_2 \\ V_3 \\ V_4 \\ V_5 \\ V_6 \\ V_7 \\ V_8 \\ V_9 \end{bmatrix} = \begin{bmatrix} 0 \\ 0 \\ 0 \\ 0 \\ 0 \\ 0 \\ 1 \\ 1 \\ 1 \end{bmatrix}$$

Figure 5: The matrix equation of grid space shown in ***Error! Reference source not found.****.*

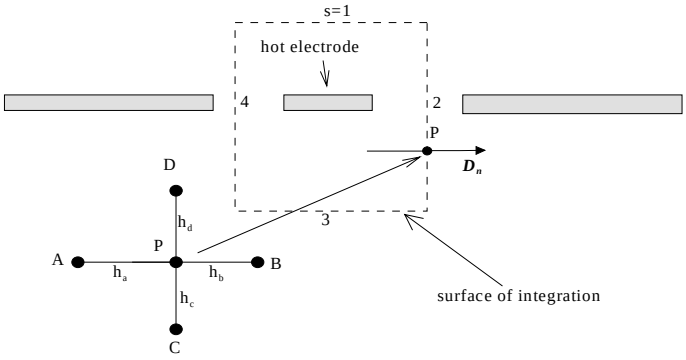

Figure 6: Integration surface for determine charge

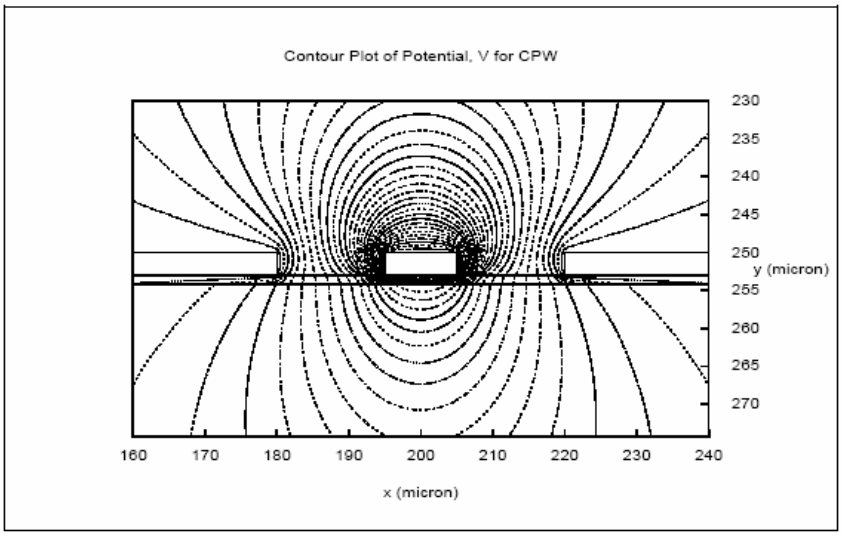

Figure 7(a): Contour plot of the Laplace Equation Solution for the CPW electrodes structure

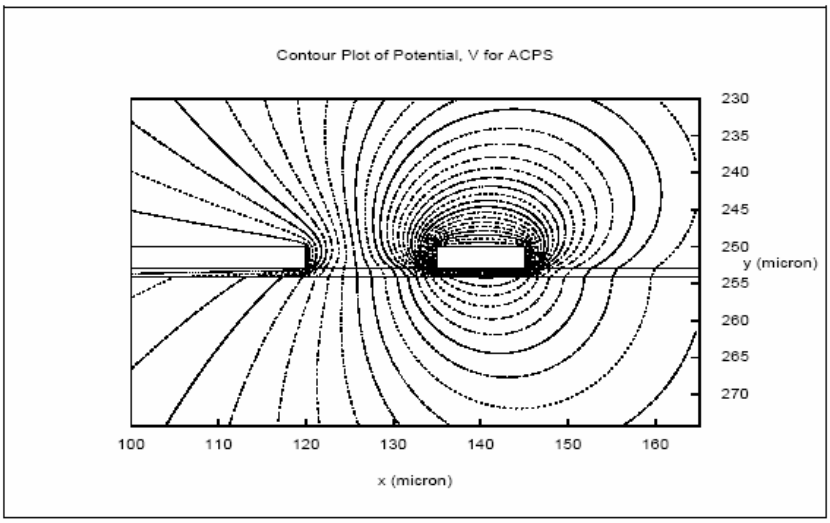

Figure 7 (b): Contour plot of the Laplace Equation Solution for the ACPS electrodes structure

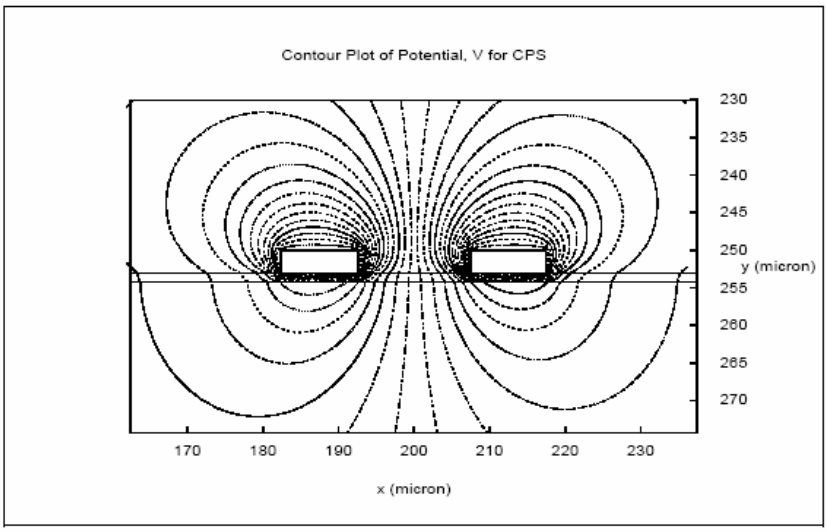

Figure 7 (c): Contour plot of the Laplace Equation Solution for the CPS electrodes structure

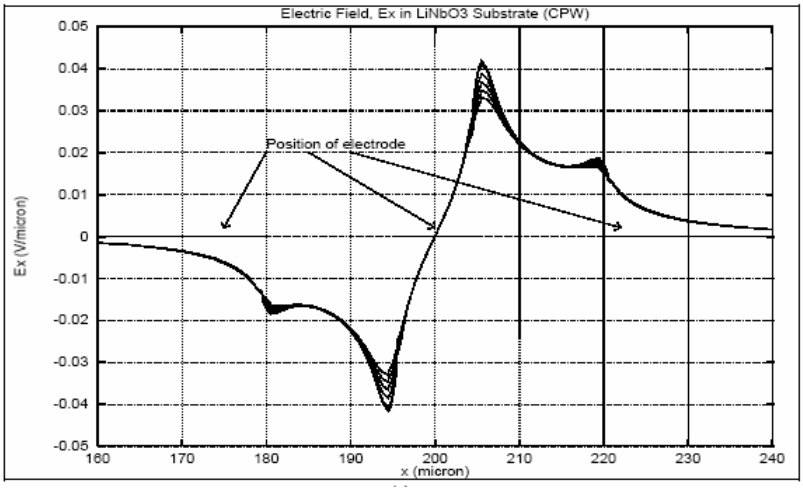

(a)

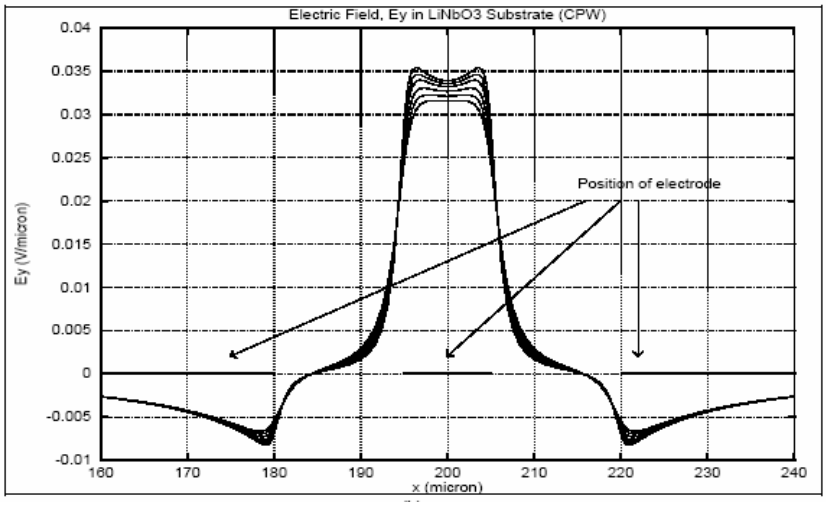

(b)

Figure 8: Electric Field (a) E_x and (b) E_y of the CPW electrode from the first 1 μm of $LiNbO_3$ just beneath the SiO_2 buffer layer.

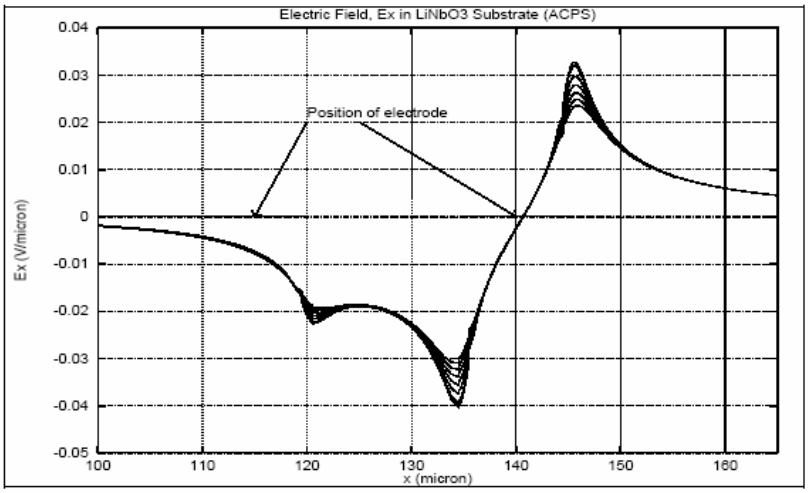

(a)

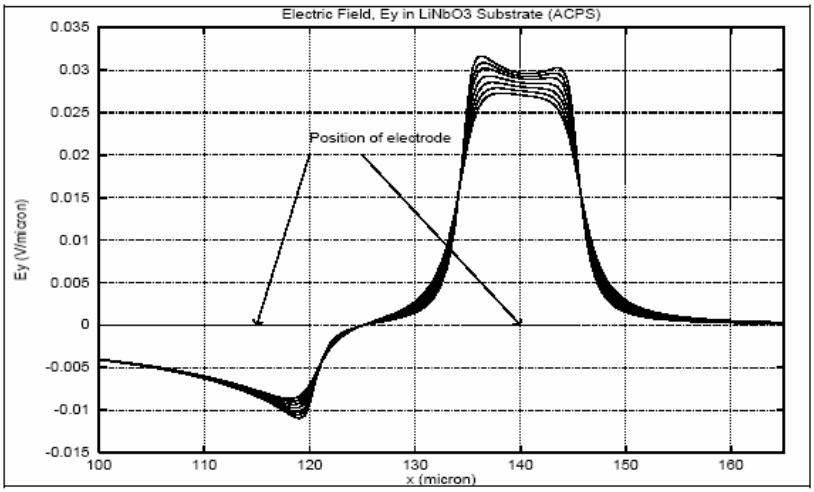

(b)

Figure 9: Electric Field (a)E_x and (b)E_y of ACPS electrode from the first 1 μm of $LiNbO_3$ just beneath the SiO_2 buffer layer.

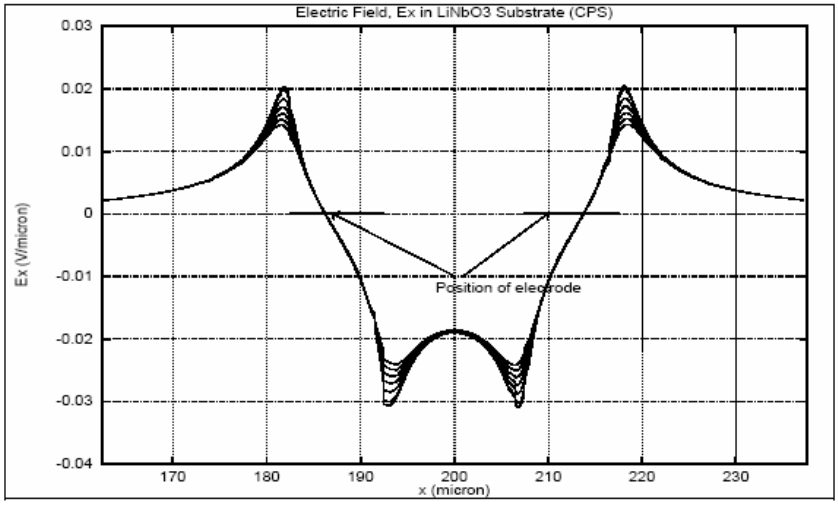

(a)

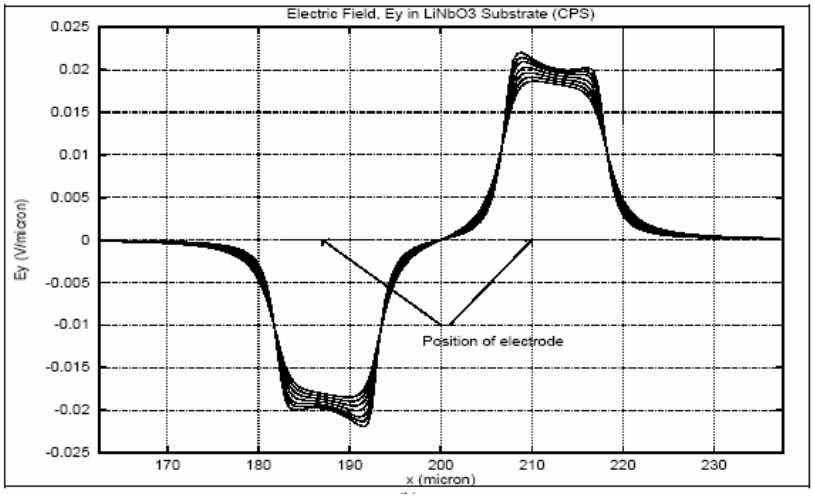

(b)

Figure 10: Electric Field a)E_x and b)E_y of CPS electrode from the first 1 μm of $LiNbO_3$ just beneath the SiO_2 buffer layer.

Ref. No	*Structure*	*w(μm)*	*g(μm)*	*t(μm)*	*t_b(μm)*	*Published*		*FDTWEA*	
						n_m	*$Z(\Omega)$*	*n_m*	*$Z(\Omega)$*
Chung[5]	*CPW*	*20*	*5*	*3*	*0.6-0.85*	*2.7*	*27*	*2.867-2.703*	*27-27.3*
	CPW	*48*	*10*	*3*	*0.6-0.85*	*3.3*	*24.5*	*3.358-3.224*	*24.13-214*
Korotky[22]	*ACPS*	*15*	*5*	*4*	*0*	*-*	*~35*	*3.661*	*29.83*
		15	*5*	*0*	*0*	*-*	*-*	*4.226*	*3315*
Chuang[16]	*ACPS*	*10*	*10*	*1.5*	*0.1*	*-*	*45(Cal)* *47.1(TDR)* *49.8(NA)*	*3.781*	*427*

Table 1: FDTWEA's calculation compare with the published results

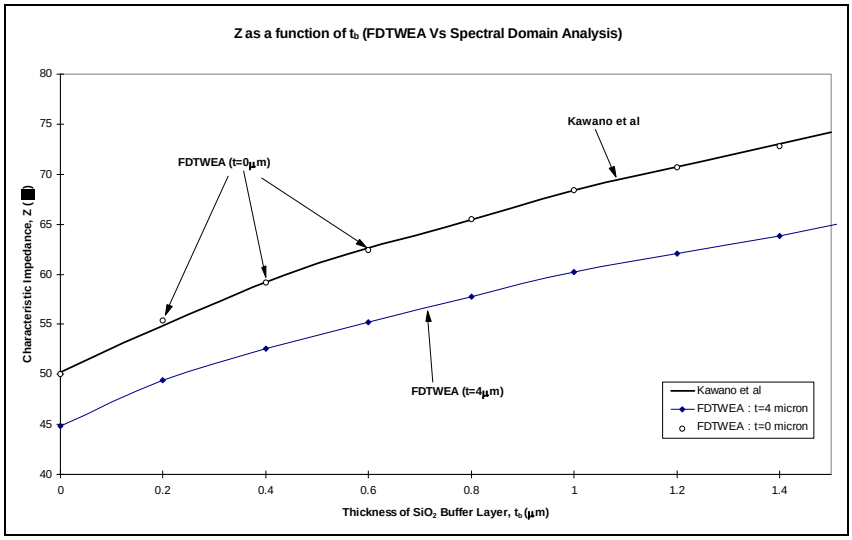

Figure 11(a): Impedance calculation of FDTWEA compared to that of the Spectral Domain Analysis

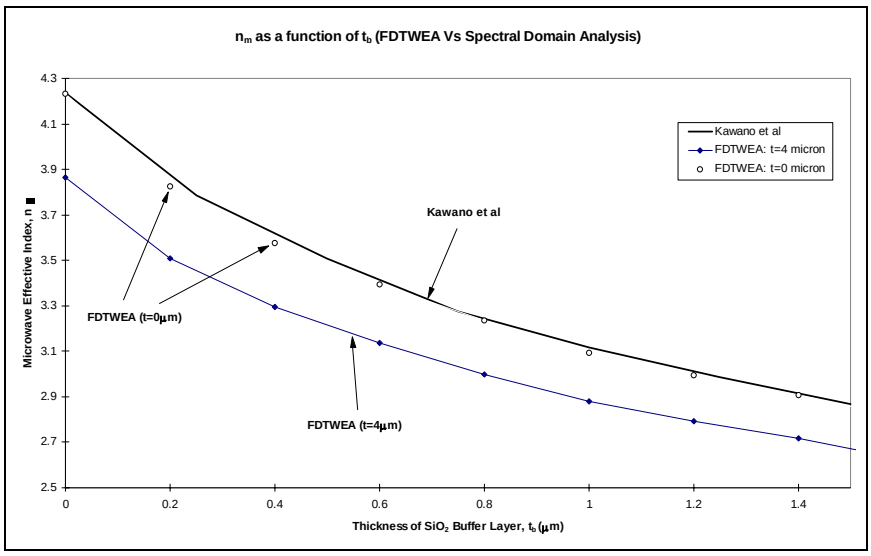

Figure 11 (b): Calculation of n_m by FDTWEA compared to that of Spectral Domain analysis

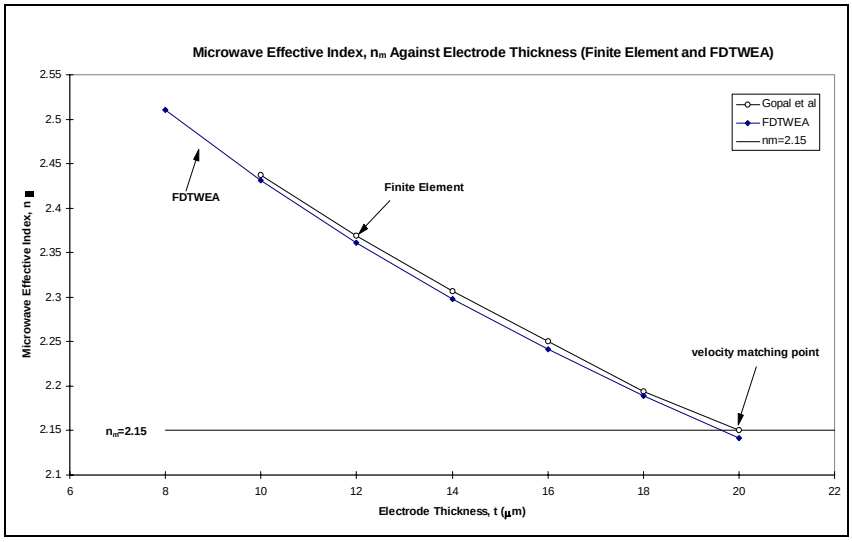

Figure 12: FDTWEA's calculation of n_m compares with the Finite Element Method.

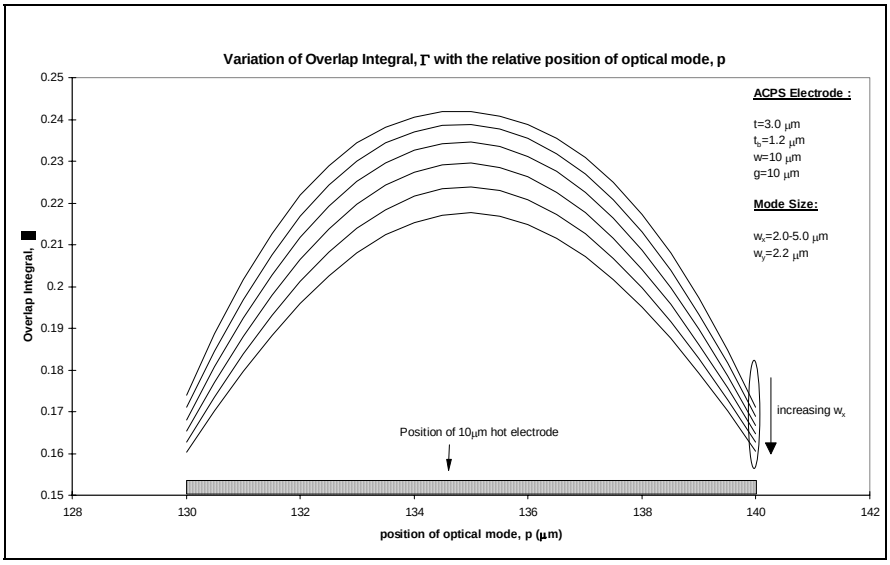

Figure 13: Variation of Γ as the peak position of the optical mode shift from one end of the hot electrode to another for increasingly wider optical mode

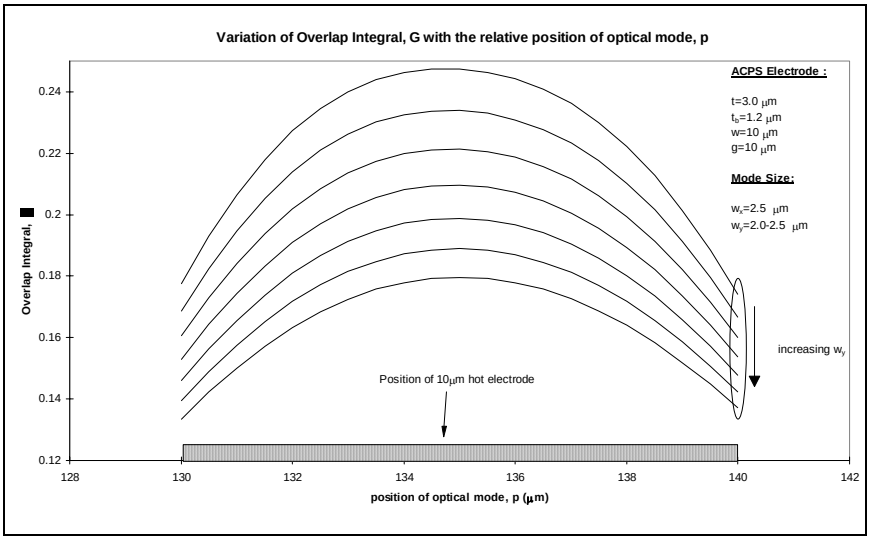

Figure 14: Variation of Γ as the peak position of the optical mode shift from one end of the hot electrode to another for increasingly deeper optical mode

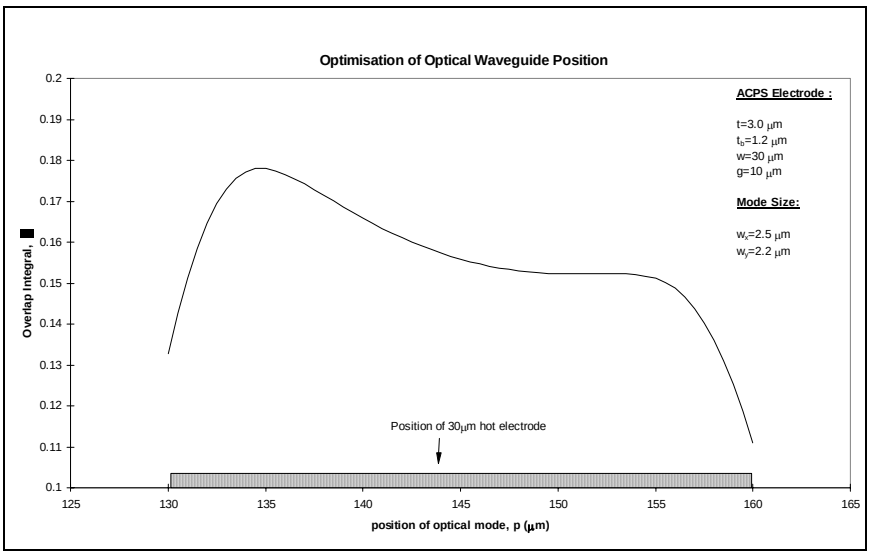

Figure 15 : Consideration of waveguide position for wider electrodes

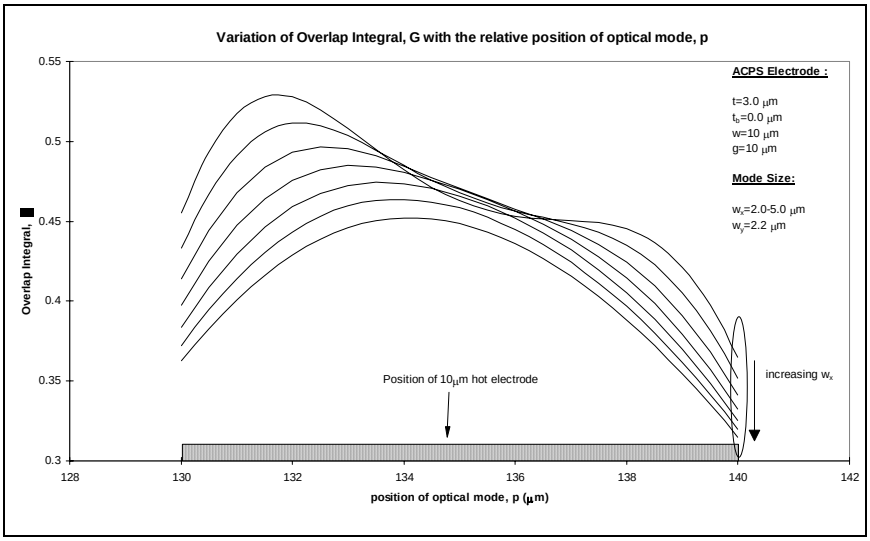

Figure 16 : Variation of Γ as the peak position of the optical mode shift from one end of the hot electrode to another for increasing wider optical mode for electrode with no buffer layer, t_b=0

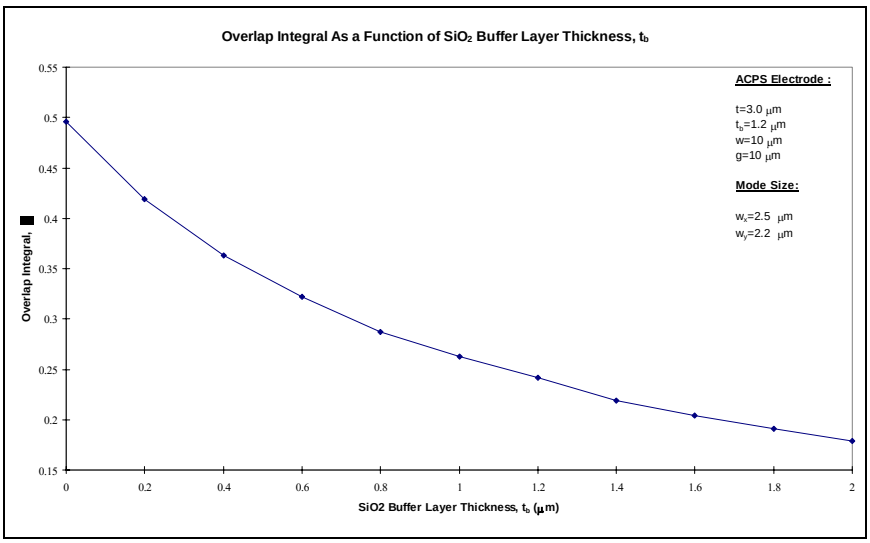

Figure 17: Γ as a function of the thickness of SiO_2 buffer, t_b

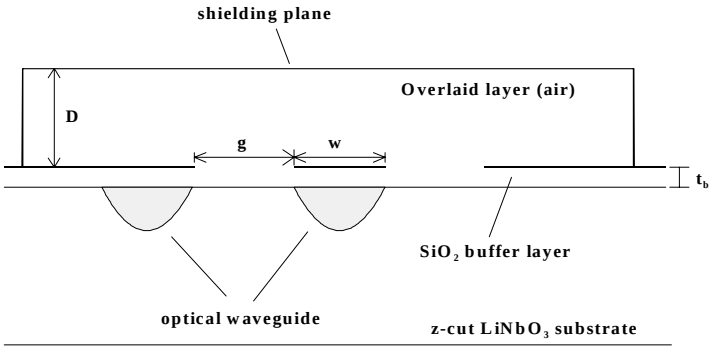

Figure 18: Schematic view of proposed phase velocity matching Mach-Zehnder optical Modulator[11-12]

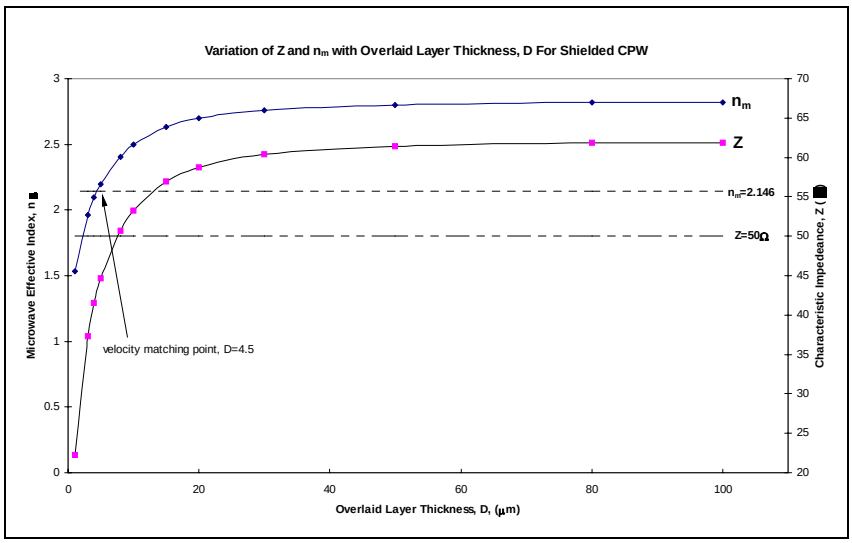

Figure 19 : Calculated microwave effective index, n_m, characteristic impedance, Z as functions of overlaid layer thickness, D.

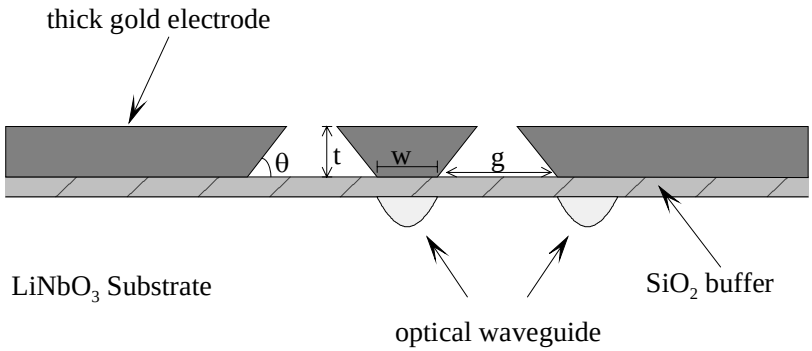

Figure 20: Wall Angle of Thick Electrodes

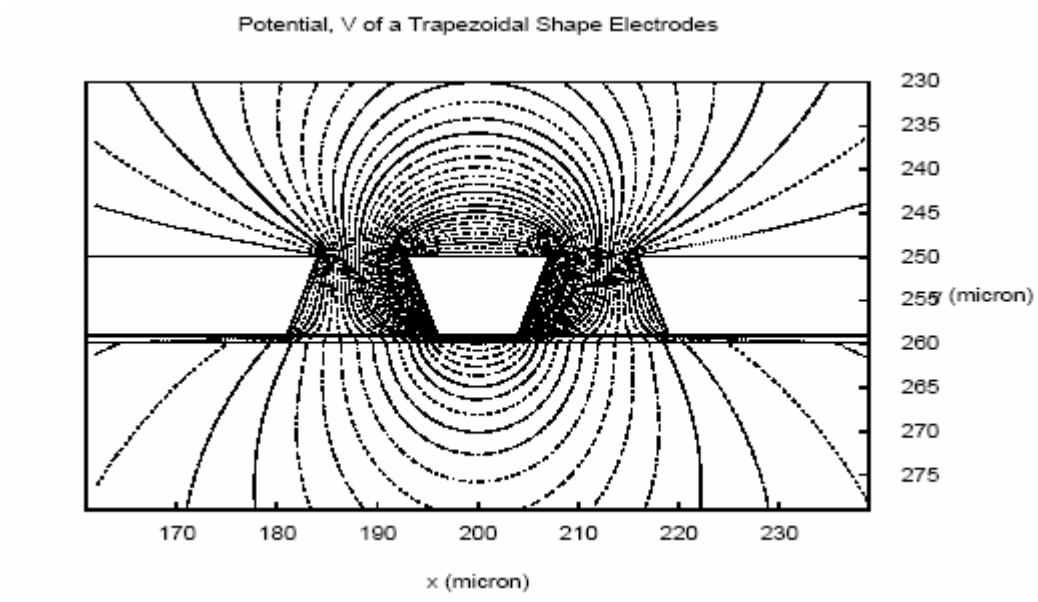

Figure 21: The potential profile of the trapezoidal shape electrode.

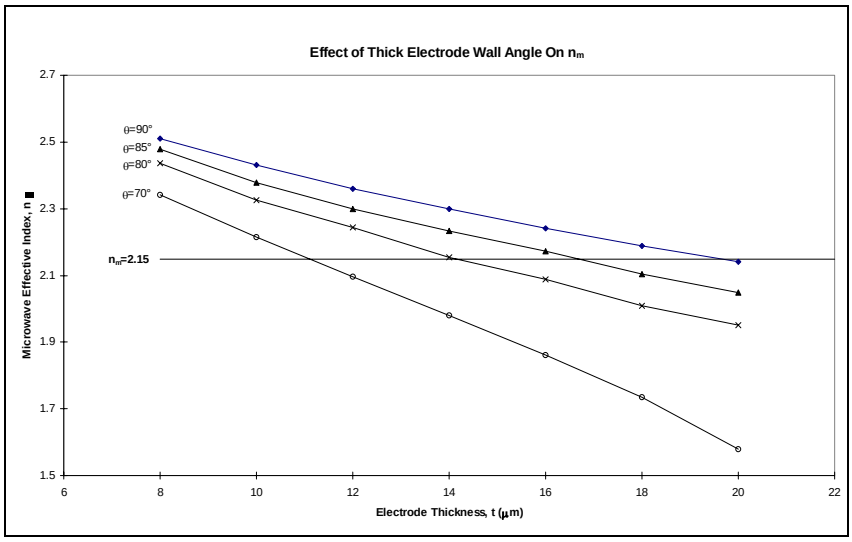

Figure 21: FDTWEA simulations of wall angle dependence on n_m.

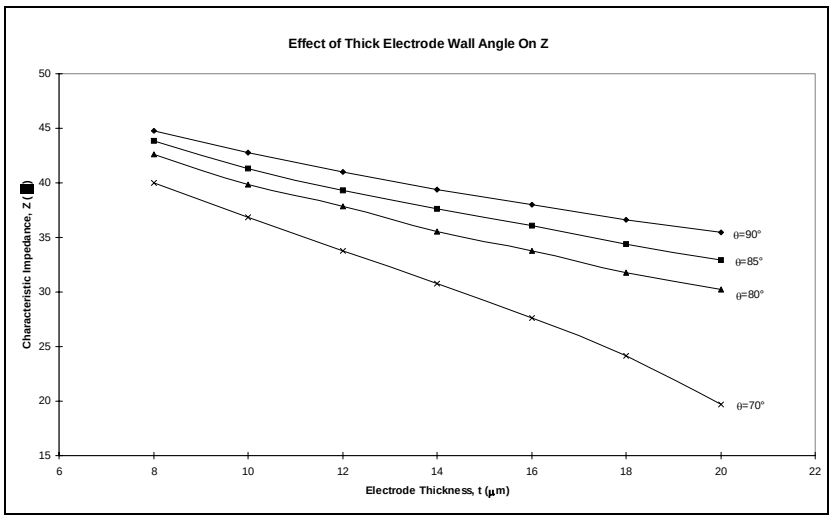

Figure 22: FDTWEA simulations of wall angle dependence